LETTERS
PUBLISHED ONLINE: 23 OCTOBER 2017 | DOI: 10.1038/NNANO.2017.198
nature nanotechnology

Direct measurement of Kramers turnover with a levitated nanoparticle

Loïc Rondin[1†], Jan Gieseler[1†], Francesco Ricci[2], Romain Quidant[2,3], Christoph Dellago[4,5] and Lukas Novotny[1*]

Understanding the thermally activated escape from a metastable state is at the heart of important phenomena such as the folding dynamics of proteins[1,2], the kinetics of chemical reactions[3] or the stability of mechanical systems[4]. In 1940, Kramers calculated escape rates both in the high damping and low damping regimes, and suggested that the rate must have a maximum for intermediate damping[5]. This phenomenon, today known as the Kramers turnover, has triggered important theoretical and numerical studies[6]. However, as yet, there is no direct and quantitative experimental verification of this turnover. Using a nanoparticle trapped in a bistable optical potential, we experimentally measure the nanoparticle's transition rates for variable damping and directly resolve the Kramers turnover. Our measurements are in agreement with an analytical model that is free of adjustable parameters. The levitated nanoparticle presented here is a versatile experimental platform for studying and simulating a wide range of stochastic processes and testing theoretical models and predictions.

The Kramers turnover is relevant in many fields of study, including the folding dynamics of proteins[1,2], the kinetics of chemical reactions[3], or current switching in Josephson tunnel junctions[7]. However, despite its long history and extensive theoretical work, experimental attempts to observe the Kramers turnover remain sparse. For example, experiments involving Josephson tunnel junctions verified Kramers' theoretical predictions in the underdamped regime[8] and highlighted the existence of different damping regimes, but systematic errors prevented precise measurements of the transition rates in the turnover region[7]. Kramers' theory has also been investigated using molecular isomerization, where the damping was controlled through the solvent density[9]. However, such experiments could only be performed in a limited damping range, with a restricted set of parameters and no absolute knowledge about the potential energy surface, which prevented a quantitative analysis and an unambiguous experimental verification of Kramers turnover. In contrast, experiments using trapped particles in water provided quantitative results[10], but only for the overdamped case, and without resolving the Kramers turnover. Inspired by recent trapping experiments in vacuum[11–14], we extend previous measurements into the underdamped regime for a particle in a double-well trap. Because the damping coefficient Γ of a nanoparticle is proportional to the buffer gas pressure[12], P_{gas}, we are able to tune the system's damping over several orders of magnitude by adjusting the gas pressure. This control, together with an accurate knowledge of the trapping potential, allows us to determine the rates for well-to-well transitions in both the underdamped and overdamped regimes for the same particle, thereby experimentally revealing Kramers turnover for the first time.

The experimental configuration is presented in Fig. 1a. A 68-nm-radius silica particle is trapped in an optical double-well potential inside a vacuum chamber of variable pressure. The potential is formed by a pair of strongly focused infrared laser beams. The particle's three-dimensional trajectory is measured interferometrically with balanced split detection[12] using an additional weakly focused $\lambda = 532$ nm laser beam (Supplementary Section 1). This approach allows us to resolve the fast dynamics of the particle (typically on the order of 100 kHz) and measure its time-dependent position $\mathbf{r}(t)$ with high accuracy. Particle position time traces are recorded at 2 Msamples s^{-1}, for 120 s, which is longer than the thermalization time $1/\Gamma$ for all dampings considered in this work. Therefore, the distribution of particle positions $\rho(\mathbf{r})$, which we obtain by histogramming the time traces, is thermalized. We can therefore retrieve the optical potential $U(\mathbf{r})$ from the relation $\rho(\mathbf{r}) = Z^{-1}\exp[-U(\mathbf{r})/k_{\mathrm{B}}T]$, where Z is a normalization constant, k_{B} the Boltzmann constant, and T is the bath temperature (see Methods).

One challenge of the present experiment compared to previous experiments involving optically levitated nanoparticles is the large volume visited by the particle (typically 1 μm^3), which makes the measurement scheme highly nonlinear. To obtain an accurate description of the potential, we first characterize the detection scheme and account for nonlinearities present for large deviations of particle position from the origin (Supplementary Section 2). The reconstructed potential corresponds to the actual potential experienced by the particle, accounting for any misalignments as well as possible perturbations arising from the measurement beam. As an example, a two-dimensional (2D) cross-section of the measured potential is shown in Fig. 1b, highlighting the presence of two stable wells A and C (black dots in the figure) and one saddle point B (black square). Important physical parameters for the description of the particle dynamics can be extracted from the measured optical potential. Near the stable and saddle points the potential is locally harmonic. Thus, a local harmonic fit around these points provides the characteristic frequencies ω_i^{A}, ω_i^{B} and ω_i^{C}, where index i indicates the local principal axis ($i \in \{x', y', z'\}$)[10].

Among the three characteristic frequencies at the saddle point, $\omega_{y'}^{\mathrm{B}}$ is purely imaginary and is denoted $\omega_{\mathrm{S}}^{\mathrm{B}}$ in the following given its importance. This curvature is associated with an unstable normal mode, and determines the transition from the underdamped to the overdamped regime. Roughly, the turnover is expected to occur for a damping at which the energy dissipated when moving

[1]ETH Zürich, Photonics Laboratory, 8093 Zürich, Switzerland. [2]ICFO-Institut de Ciencies Fotoniques, The Barcelona Institute of Science and Technology, 08860 Castelldefels (Barcelona), Spain. [3]ICREA-Institució Catalana de Recerca i Estudis Avançats, 08010 Barcelona, Spain. [4]Faculty of Physics, University of Vienna, Boltzmanngasse 5, 1090 Wien, Austria. [5]Erwin Schrödinger International Institute for Mathematics and Physics, University of Vienna, Boltzmanngasse 9, 1090 Wien, Austria. †Present address: Laboratoire Aimé Cotton, CNRS, Université Paris-Sud, ENS Cachan, Université Paris-Saclay, 91405 Orsay Cedex, France (L.R.); Physics Department, Harvard University, Cambridge, Massachusetts 02318, USA (J.G.). *e-mail: lnovotny@ethz.ch

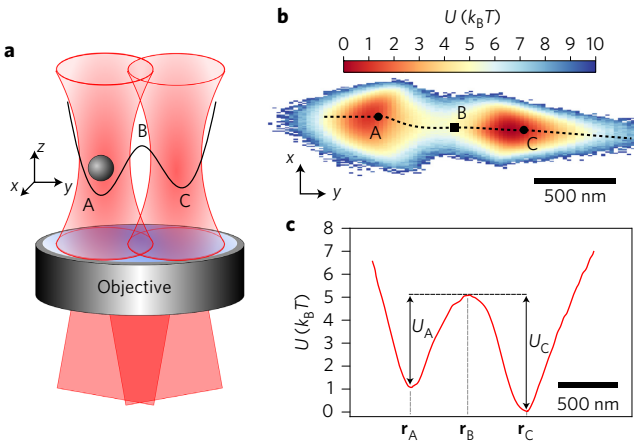

Figure 1 | Double-trap set-up. a, Two focused infrared beams generate an optical potential with two wells (A and C), linked by a saddle point B. The experiment is operated inside a vacuum chamber. **b**, Two-dimensional cross-section of the reconstructed optical potential in the transverse (x–y) plane. The double-well potential has two stable stationary points A and C, and an unstable stationary point B. The dotted line represents the minimum energy path between points A and C. **c** Trapping potential evaluated along the dotted line in **b**. The potential energy barriers U_A and U_C are resolved clearly.

accross the barrier is of the order of the thermal energy k_BT. For a barrier consisting of an inverted parabola with a curvature determined by ω_S^B, this condition yields $\Gamma/|\omega_S^B| \approx k_BT/U_b$, where U_b is the energy barrier[6]. Experimentally, we measure the energy barriers $U_A \approx 4k_BT$ and $U_C \approx 5k_BT$ as well as $|\omega_S^B|/2\pi \approx 51$ kHz. Consequently, because $\Gamma/P_{gas} \approx 51$ Hz Pa^{-1}, we expect the turnover to occur at a gas pressure in the range of $P_{gas} \approx 1{,}200$–$1{,}600$ Pa. In addition, we estimate the minimum energy path of the measured potential by using a steepest gradient algorithm (Fig. 1c). Following the minimum energy path we then evaluate the particle's action S over one oscillation period. The action S will be important later when we discuss the theoretical derivation of the particle's jumping rates.

Besides the reconstruction of the optical potential, we use the time traces of the particle position to determine the jumping rates between the wells. Figure 2a–c presents typical time traces projected along the y axis (double-well axis), recorded for different gas pressures. The time traces clearly show the expected bistable behaviour. Moreover, the jumping rates change with gas pressure, as expected from Kramers' rate theory. To confirm this observation we analysed the kinetics in greater detail. In the underdamped regime, the energy lost by the particle during one oscillation period is small, and hence once the particle has crossed the energy barrier it can recross it multiple times, before being retrapped in one of the two wells. Conversely, in the overdamped regime, the particle loses energy quickly, and recrossing occurs only if the particle diffuses near the saddle point. To eliminate the effect of correlated recrossings, we derive the jumping rate R from the time autocorrelation of the binary population function $h_A(t)$, which is unity if the y component of the particle position at time t is negative ($y(t) < 0$), that is, if the particle is in well A, and zero otherwise (Supplementary Section 3). For kinetics governed by a rate equation, the time autocorrelation function $\langle \delta h_A(0) \delta h_A(t) \rangle$ is expected to exhibit an exponential decay at long times after an initial transient behaviour caused by correlated recrossings[15,16]. Here $\delta h_A = h_A - \langle h_A \rangle$ is the deviation of h_A from its long time average $\langle h_A \rangle$. By fitting the exponential decay e^{-Rt} to $\langle \delta h_A(0) \delta h_A(t) \rangle$ we determine the jumping rate constant R (Fig. 2d), which equals the sum of the rate constants for the forward and backward processes, $R = R_{AC} + R_{CA}$. Note that R is the relaxation rate of a non-equilibrium population in the wells towards equilibrium. Besides removing correlated recrossings, this approach provides rates that are independent of the exact choice of the barrier separating the two stable wells A and C.

To observe the Kramers turnover we record the dynamics of the particle over a wide range of pressures and hence dampings Γ. The chamber pressure P_{gas} is lowered to 200 Pa ($\Gamma \approx 10$ kHz $\ll |\omega_S^B| k_BT/U_b$), and increased stepwise to 2×10^4 Pa ($\Gamma \approx 1$ MHz $\gg |\omega_S^B| k_BT/U_b$). At each pressure step, the potential and jumping rate are computed from time traces of the particle motion, as discussed previously. The measured rates are shown in Fig. 3. The particle jumping rate clearly exhibits a maximum, near $\Gamma \approx |\omega_S^B| k_BT/U_b$.

The experimentally determined optical potential allows us to quantitatively compare our measurements with theoretical models that have been developed during recent decades[6,17,18]. In the overdamped regime, multidimensional rate theory, which has been studied intensively theoretically[19] and verified experimentally[10,20], yields

$$R_{AC}^{HD} = \frac{1}{2\pi} \prod_{i \in \{x,y,z\}} \frac{\omega_i^A}{|\omega_i^B|} \left[\sqrt{|\omega_B^S|^2 + \frac{\Gamma^2}{4}} - \frac{\Gamma}{2} \right] e^{\frac{U_A}{k_BT}} \quad (1)$$

for the transition from well A to C. The reverse rate R_{CA}, for the transition from well C to A, is obtained by swapping the indices A and C. For a given barrier height, the rate constant decreases with increasing damping and becomes inversely proportional to Γ in the limit of high friction due to slow diffusion of the system across the barrier.

In the underdamped regime, on the other hand, the rate-limiting factor is the slow transfer of energy between system and bath, leading to a rate proportional to Γ. Although the jumping rates in the two limiting cases were already derived by Kramers, a full analytical theory bridging the underdamped and overdamped regimes was obtained only much later[17]. To cross over from the overdamped to the underdamped case, one introduces the depopulation factor

$$\Upsilon(\delta) = \exp\left[\frac{1}{\pi} \int_0^\infty \ln\left\{ 1 - \exp\left[-\frac{\delta}{k_BT} \left(x^2 + \frac{1}{4} \right) \right] \right\} \frac{dx}{x^2 + \frac{1}{4}} \right] \quad (2)$$

where δ is the energy loss parameter and the integration is carried out over the positive part of the real axis[6,17]. The estimation of this energy loss parameter is one of the major challenges in the context of Kramers turnover theories[18]. However, in our experimental situation, where the friction is memory-free, this energy loss is well approximated by $\delta = \Gamma S$, where $S = S_A$ (resp. S_C) is the particle action over one oscillation for the particle in well A (resp. C)[17]. The action is then measured along the minimum energy path of the potential, shown in Fig. 1b,c, from A to B (resp. C to B) (see Methods). In the case of a double-well potential, due to the recrossing dynamics, the probability of the particle being retrapped in trap A is different from that in trap C. The correct rate expression for the rate dynamics, for any damping, requires that these different probabilities be taken into account. The transition rate from A to C is thus obtained by multiplying the high damping transition rate R_{AC}^{HD} (equation (1)) by the factor $\Upsilon(\Gamma S_A)\Upsilon(\Gamma S_C)/\Upsilon(\Gamma S_A + \Gamma S_C)$[6,17]. Finally, our rate estimates, based on measuring the autocorrelation of the particle's time traces, yields the sum of the rates A → C and C → A. Therefore, the expected theoretical jumping rate constant is

$$R(\Gamma) = \frac{\Upsilon(\Gamma S_A)\Upsilon(\Gamma S_C)}{\Upsilon(\Gamma S_A + \Gamma S_C)} \left[R_{AC}^{HD} + R_{CA}^{HD} \right] \quad (3)$$

which is valid in the entire range from low to high friction.

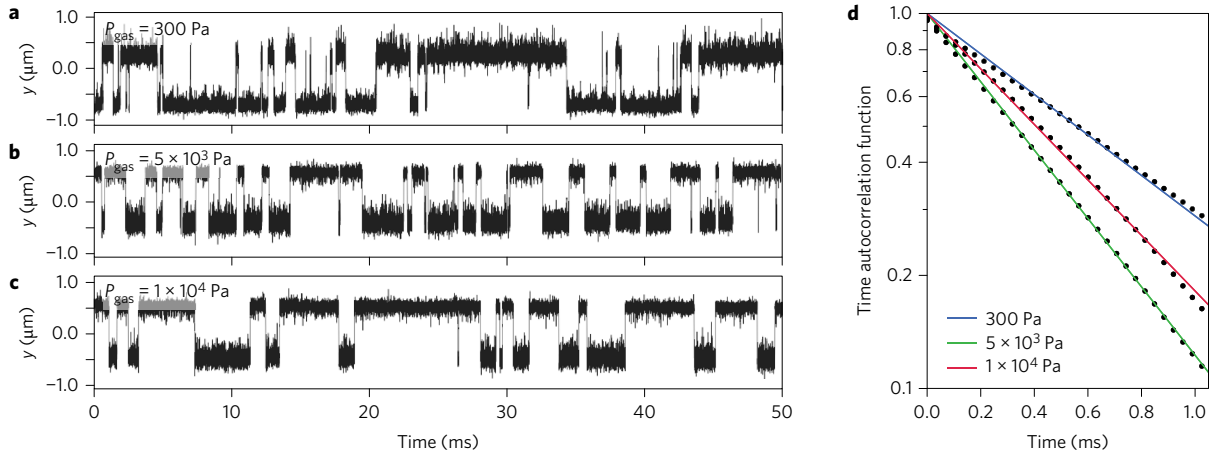

Figure 2 | Transition kinetics. a–c, Time traces along the double trap *y* axis taken at different pressures. **d**, Time autocorrelation functions of the population operators, $\langle \delta h_A(0) \delta h_A(t) \rangle$, obtained from the time traces. These time autocorrelations are fitted (solid coloured lines) by an exponential decay, allowing us to extract the jumping rate constant *R* for each pressure.

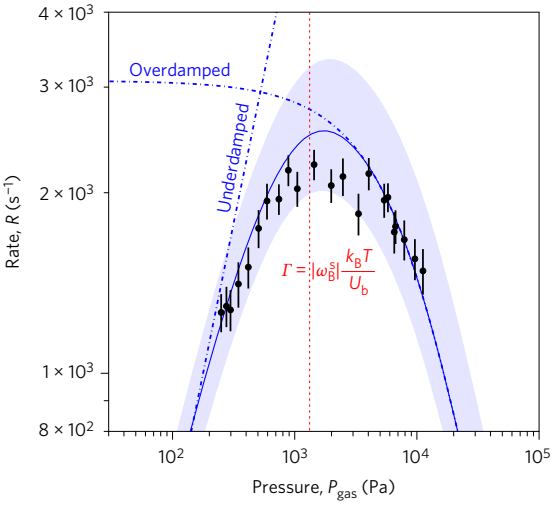

Figure 3 | Experimentally measured jumping rate *R* as a function of gas pressure P_{gas} (black dots) compared with the analytical model of equation (3). The solid blue line shows the analytical model. Error bars indicate standard deviations obtained by measuring the autocorrelation over 100 different time traces of 0.5 s. The blue shaded area indicates the uncertainty of the theoretical model due to parameter variations. The red line highlights the condition $\Gamma/|\omega_B^S| = k_B T/U_b$, where U_b is an effective barrier height, corresponding to an average over the barrier heights measured for both trap A and C. Dash-dotted lines highlight the two limiting cases of low and high damping (see Methods).

To mitigate the influence of small changes in experimental parameters (for example, due to drift), the optical potential is measured for each pressure step, and the experimental parameters used in the rate analysis (equation (3)) are determined independently for each pressure (see Methods and Supplementary Section 4). To compare the analytical model with our measurements, we average the parameters obtained for different pressures and use them in equation (3). The resulting rate is presented in Fig. 3 (solid blue line). We then calculate the uncertainties of the model by evaluating the ensemble of the measured parameters over the whole set of pressures. These uncertainties are shown as a blue shaded area. Our experimental data always fall within the uncertainty and agree with the prediction obtained with averaged parameters to within less than 20%. This small mismatch between theory and experiment is caused by uncertainties in the determination of the exact shape of the potential, as well as drifts associated with the measurement beam, which are more pronounced at higher pressures (see Supplementary Section 6 for details). Nevertheless, our results give strong support to the analytical model presented in equation (3). We anticipate that improvements in the stability of the set-up, especially by having precise pressure and temperature control in addition to improved detection, will further enhance the agreement.

The laser-trapped nanoparticle serves as a statistical simulator that allows us to study rate theories in complex systems. The particle dynamics can be studied in time-dependent arbitrary three-dimensional energy landscapes that can be created by optical point-spread-function engineering[21]. We can also study non-ohmic friction by applying correlated noise to the trapping beams. Thus, our system provides an experimental testboard for a large variety of physical models. In addition, theoretically challenging non-equilibrium dynamics can be addressed easily with our statistical simulator, either by applying noise to the trapping potential[22], or by preparation of non-thermal states[13]. This enables the study of different noise-induced phenomena, such as stochastic resonance[23,24], in any damping regime. Finally, given the recent advances towards quantum ground-state cooling of vacuum-trapped particles[25–27], we expect that our system will provide a way to shed light on rate theories at the classical to quantum transition. This ability to test the applicability and the potential breakdown of escape rate models is of crucial interest to understand and interpret experiments. To summarize, using an optically trapped nanoparticle in vacuum, we directly measured the Kramers turnover. The experimental approach provides the quantitative data needed to test multidimensional rate theories and explore the parameters that influence the escape dynamics from single potentials and hopping between stable wells. Due to the fine control of the system parameters, our experimental simulator can be used to study switching dynamics and validate rate models in a wide range of system–bath couplings, shining light on problems ranging from protein folding[2] to diffusion in solids[28]. Also, the experimental platform is well suited for studying open questions in non-equilibrium and non-Markovian statistical physics, in particular in situations where Brownian dynamics is influenced by different damping regimes. Such studies will benefit the development of optimal protocols for the conversion between information and energy[29,30] and stochastic heat engines[31].

Methods

Methods and any associated references are available in the online version of the paper.

Received 12 December 2016; accepted 23 August 2017; published online 23 October 2017

References

1. Best, R. & Hummer, G. Diffusive model of protein folding dynamics with Kramers turnover in rate. *Phys. Rev. Lett.* **96,** 228104 (2006).
2. Chung, H. S., Piana-Agostinetti, S., Shaw, D. E. & Eaton, W. A. Structural origin of slow diffusion in protein folding. *Science* **349,** 1504–1510 (2015).
3. Garcìa-Müller, P. L., Borondo, F., Hernandez, R. & Benito, R. M. Solvent-induced acceleration of the rate of activation of a molecular reaction. *Phys. Rev. Lett.* **101,** 178302 (2008).
4. Badzey, R. L. & Mohanty, P. Coherent signal amplification in bistable nanomechanical oscillators by stochastic resonance. *Nature* **437,** 995–998 (2005).
5. Kramers, H. Brownian motion in a field of force and the diffusion model of chemical reactions. *Physica* **7,** 284–304 (1940).
6. Hänggi, P., Talkner, P. & Borkovec, M. Reaction-rate theory: fifty years after Kramers. *Rev. Mod. Phys.* **62,** 251–341 (1990).
7. Silvestrini, P., Pagano, S., Cristiano, R., Liengme, O. & Gray, K. E. Effect of dissipation on thermal activation in an underdamped Josephson junction: first evidence of a transition between different damping regimes. *Phys. Rev. Lett.* **60,** 844–847 (1988).
8. Turlot, E. *et al.* Escape oscillations of a Josephson junction switching out of the zero-voltage state. *Phys. Rev. Lett.* **62,** 1788–1791 (1989).
9. Schroeder, J., Troe, J. & Vöhringer, P. Photoisomerization of trans-stilbene in compressed solvents: Kramers-turnover and solvent induced barrier shift. *Z. Phys. Chem.* **188,** 287–306 (1995).
10. McCann, L. I., Dykman, M. & Golding, B. Thermally activated transitions in a bistable three-dimensional optical trap. *Nature* **402,** 785–787 (1999).
11. Li, T., Kheifets, S., Medellin, D. & Raizen, M. G. Measurement of the instantaneous velocity of a Brownian particle. *Science* **328,** 1673–1675 (2010).
12. Gieseler, J., Deutsch, B., Quidant, R. & Novotny, L. Subkelvin parametric feedback cooling of a laser-trapped nanoparticle. *Phys. Rev. Lett.* **109,** 103603 (2012).
13. Gieseler, J., Quidant, R., Dellago, C. & Novotny, L. Dynamic relaxation of a levitated nanoparticle from a non-equilibrium steady state. *Nat. Nanotech.* **9,** 358–364 (2014).
14. Millen, J., Deesuwan, T., Barker, P. & Anders, J. Nanoscale temperature measurements using non-equilibrium Brownian dynamics of a levitated nanosphere. *Nat. Nanotech.* **9,** 425–429 (2014).
15. Chandler, D. Statistical mechanics of isomerization dynamics in liquids and the transition state approximation. *J. Chem. Phys.* **68,** 2959–2970 (1978).
16. Dellago, C. & Bolhuis, P. G. in *Advanced Computer Simulation Approaches for Soft Matter Sciences III* (eds Holm, P. C. & Kremer, P. K.) 167–233 (Springer, 2009).
17. Mel'nikov, V. I. The Kramers problem: fifty years of development. *Phys. Rep.* **209,** 1–71 (1991).
18. Pollak, E. & Ankerhold, J. Improvements to Kramers turnover theory. *J. Chem. Phys.* **138,** 164116 (2013).
19. Hershkovitz, E. & Pollak, E. Multidimensional generalization of the Pollak–Grabert–Haenggi turnover theory for activated rate processes. *J. Chem. Phys.* **106,** 7678–7699 (1997).
20. Han, S., Lapointe, J. & Lukens, J. E. Thermal activation in a two-dimensional potential. *Phys. Rev. Lett.* **63,** 1712–1715 (1989).
21. Bowman, R. W. & Padgett, M. J. Optical trapping and binding. *Rep. Prog. Phys.* **76,** 026401 (2013).
22. Dykman, M. I. & Ryvkine, D. Activated escape of periodically modulated systems. *Phys. Rev. Lett.* **94,** 070602 (2005).
23. Gammaitoni, L., Hänggi, P., Jung, P. & Marchesoni, F. Stochastic resonance. *Rev. Mod. Phys.* **70,** 223–287 (1998).
24. Ricci, F. *et al.* Optically levitated nanoparticle as a model system for stochastic bistable dynamics. *Nature Commun.* **8,** 15141 (2017).
25. Kiesel, N. *et al.* Cavity cooling of an optically levitated submicron particle. *Proc. Natl Acad. Sci. USA* **110,** 14180–14185 (2013).
26. Fonseca, P. Z. G., Aranas, E. B., Millen, J., Monteiro, T. S. & Barker, P. F. Nonlinear dynamics and strong cavity cooling of levitated nanoparticles. *Phys. Rev. Lett.* **117,** 173602 (2016).
27. Jain, V. *et al.* Direct measurement of photon recoil from a levitated nanoparticle. *Phys. Rev. Lett.* **116,** 243601 (2016).
28. Guantes, R., Vega, J. L., Miret-Artes, S. & Pollak, E. Kramers turnover theory for diffusion of Na atoms on a Cu(001) surface measured by He scattering. *J. Chem. Phys.* **119,** 2780–2791 (2003).
29. Toyabe, S., Sagawa, T., Ueda, M., Muneyuki, E. & Sano, M. Experimental demonstration of information-to-energy conversion and validation of the generalized Jarzynski equality. *Nat. Phys.* **6,** 988–992 (2010).
30. Bérut, A. *et al.* Experimental verification of Landauer's principle linking information and thermodynamics. *Nature* **483,** 187–189 (2012).
31. Dechant, A., Kiesel, N. & Lutz, E. All-optical nanomechanical heat engine. *Phys. Rev. Lett.* **114,** 183602 (2015).

Acknowledgements

This research was supported by the Swiss National Science Foundation (no. 200021L_169319) in cooperation with the Austrian Science Fund (no. I 3163), ERC-QMES (no. 338763), CoG ERC-QnanoMECA (no. 64790), Fundació Privada CELLEX and the severo Ochoa programme. L.R. acknowledges support from an ETH – Marie Curie Cofund Fellowship. The authors thank M. Frimmer, V. Jain, E. Hebestreit, C. Moritz, P. Mestres, E. Pollak and P. Bharadwaj for discussions and experimental support.

Author contributions

L.R. and L.N. designed and conceived the experiment. L.R. performed the experiment and analysed the data, with input from J.G., C.D. and L.N. All authors discussed the results and contributed to writing the manuscript.

Additional information

Supplementary information is available in the online version of the paper. Reprints and permissions information is available online at www.nature.com/reprints. Publisher's note: Springer Nature remains neutral with regard to jurisdictional claims in published maps and institutional affiliations. Correspondence and requests for materials should be addressed to L.N.

Competing financial interests

The authors declare no competing financial interests.

Methods

Experimental set-up. The optical double-well trap was generated using two cross-polarized and frequency-shifted (40 MHz) beams from a continuous-wave infrared laser (λ = 1,064 nm, Coherent Mephisto). Before entering the chamber, the two orthogonal polarizations are recombined using a polarizing beamsplitter (PBS) and focused by a NA = 0.8 objective (Nikon). The relative position of the two traps can be changed using a Newport fast steering mirror.

The particle position was recorded using an additional, weakly focused, green laser (λ = 532 nm, Coherent) and three balanced detectors (Newport, 1817-FC). The signal was filtered (low-pass filter at 1 MHz) before being recorded on a fast data acquisition card (Gage, Oscar CS4342). The 3D particle trajectory was reconstructed from the measured signal using a calibration function, determined independently. Additional details on the experimental set-up and measurement calibration are provided in Supplementary Sections 1 and 2.

Determination of physical parameters. *Positions of the saddle and stable points.* The optical potential is derived from the particle distribution function $\rho(\mathbf{r})$, obtained by histogramming the particle position time trace. Thus, the optical potential U at each point $\mathbf{r}$ follows from

$$U(\mathbf{r}) = -k_B T \ln[\rho(\mathbf{r})] \tag{4}$$

where k_B is the Boltzmann constant and T = 300 K is the temperature of the gas. By differentiation we obtain the effective force field $\mathbf{F}(\mathbf{r}) = -\mathbf{grad}\ U(\mathbf{r})$. The force vanishes at the two stable points A and C and at saddle point B.

Energy barriers and potential curvature. Near the saddle point and the stable points, the potential energy can be approximated by a harmonic function:

$$U_{HO}(\mathbf{r}) = U_\alpha + \frac{1}{2}\sum_{i,j} \Lambda^\alpha_{i,j}(r_i - r^\alpha_i)(r_j - r^\alpha_j) \tag{5}$$

where α = A, B or C, $\mathbf{r}^\alpha$ is the spatial position of point α, U_α is the potential energy at point α, and $i, j \in \{x, y, z\}$.

A local fit of the measured potential U_{HO} yields the matrix $(\Lambda^\alpha_{i,j})$ for each of the three spatial points. The three eigenvalues λ^α_k of each matrix correspond to the curvatures along the three local normal axes $k \in \{x', y', z'\}$ of the potential, $\omega^\alpha_k = \sqrt{\lambda^\alpha_k/m}$, where m is the mass of the particle, and the primed coordinates denote the local coordinate system. Alternatively, the full potential can be fitted by

$$\Pi_{fit}(x, y, z) = \sum_{i,j,k} \mu_{i,j,k} x^i y^j z^k \tag{6}$$

to derive the curvature in any point of the potential. Good convergence is typically obtained for a polynomial at order ~10. The results of the two different fitting procedures agree within a few percent.

Particle action. The particle action over one oscillation is approximated by the action over the minimum energy path, given by

$$S_i = 4\int_{r_i}^{r_B} \sqrt{2m[U_B - U(\mathbf{r})]}\,dr \tag{7}$$

where i = A, C.

The integration is carried out along the minimum energy path, which is the path between the two stables points A and C that minimizes the energy. We determine the minimum energy path using a steepest gradient algorithm. This path is shown in Fig. 1c. As a guide for the eye, the path in this figure has been continued beyond A and C, although there is no minimum energy path outside of the A to C range. Finally, note that the factor 4 in equation (7) originates from measuring only one-quarter of the full oscillation period.

The evolution of the recorded parameters as a function of pressure is presented in the Supplementary Information (Supplementary Fig. 7).

Low and high damping limiting cases. Figure 3 presents the theoretical limiting cases, corresponding to the low and high damping regimes (blue dash-dotted lines). The high damping rates were computed using equation (1), and the low damping rates correspond to the equation[17]

$$R^{LD} = \frac{S_A S_C}{S_A + S_C}\frac{\Gamma}{2\pi k_B T}\left(\omega^A_{y'} e^{-\frac{U_A}{k_B T}} + \omega^C_{y'} e^{-\frac{U_C}{k_B T}}\right) \tag{8}$$

Note that this equation is an approximation for the low damping regime in one dimension, and should be a good approximation for our three-dimensional case because the three normal modes are only weakly coupled[19].

Data availability. The data that support the plots within this paper and other findings of this study are available from the corresponding author upon reasonable request.